


Micro-scale chemical and physical patterns in an interface of hydrothermal dolomitization reveals the governing transport mechanisms in nature: Case of the Layens anticline, Pyrenees, France

STEPHEN CENTRELLA^{*†‡} , NICOLAS E. BEAUDOIN^{*}, HANNELORE DERLUYN^{*†‡}, GEOFFREY MOTTE^{*}, GUILHEM HOAREAU^{*}, PIERRE LANARI[‡], FRANCESCA PICCOLI[‡], CHRISTOPHE PECHEYRAN[§] and JEAN PAUL CALLOT^{*}

^{*}Universite de Pau et des Pays de l'Adour, E2S UPPA, CNRS, TOTAL, LFCR, UMS 3360, Pau, France (E-mail: centrella.stephen@univ-pau.fr)

[†]Universite de Pau et des Pays de l'Adour, E2S UPPA, CNRS, DMEX, UMR 5150, Pau, France

[‡]Institute of Geological Sciences, University of Bern, Baltzerstrasse 3, Bern, CH-3012, Switzerland

[§]Universite de Pau et des Pays de l'Adour, E2S UPPA, CNRS, IPREM, UMR 5254, Pau, France

Associate Editor – Hairuo Qing

ABSTRACT

Hydrothermal dolomitization is an important diagenetic process that occurs in tectonic environments worldwide and forms conventional reservoirs associated with ore deposits and hydrocarbon accumulation, while forming efficient reservoirs for carbon sequestration. However, the current state of knowledge about the availability and reaction rate of Mg in dolomitizing fluids fails to explain the large volumes of hydrothermal dolomites geobodies observed in extended margins or in fold-and-thrust belts. To better understand this widespread phenomenon, it is essential to recognize the governing and limiting transport mode of the dolomitizing fluid. This contribution investigates the chemical and physical patterns developed between the original calcite and the newly formed dolomite. An extensive analytical study of well-preserved dolomitization interfaces observed at outcrop scale in Callovian–Oxfordian limestones in the Layens anticline (north-western Pyrenees, France) is presented. Through the use of scanning electron microscopy, electron backscattered diffraction, X-ray microtomography, laser ablation inductively coupled plasma mass spectrometry (and mapping), the replacement related variations in elementary content, rock density, crystallographic properties and phase volumes and distribution were constrained. The results indicate a sequence of replacement, beginning with a fluid which starts to infiltrate the host rock by advection in the grain boundary network causing at the same time the replacement of calcite by diffusion-limited dissolution and associated dolomite precipitation. The progressive replacement of calcite grains by dolomite is led by dissolution inside the grain enhanced by replacement related porosity creation, leading to a progressive decrease of local calcite grain size isolated as islands until the replacement is complete. The replacement of calcite by dolomite led to a mass loss without volume change, through generation of *ca* 11 vol.% porosity. Based on analytical observations of a natural sample, a conceptual model that accounts for the transport mode governing the different steps of hydrothermal dolomitization at crystal-scale is proposed.

Keywords Dolomitization, fluid–rock interaction, porosity, replacement, trace element.

INTRODUCTION

Fluid-mediated replacement in rocks is a fundamental process defined as metasomatism, active in the crust, locally altering the mechanical and petrophysical properties of the rocks by changing its mineralogy and chemistry (Putnis, 2009). In the sedimentary diagenetic domain (<250 to 300°C), the consequences of replacement are numerous, ranging from fracking (Jamtveit *et al.*, 2000), element cycling in the crust (Whitaker *et al.*, 2004; Ague & Nicolescu, 2014), and variations in reservoir quality for geo-resources and storage (Kirschner & Barnes, 2009; Thibeau *et al.*, 2013). Dolomitization is a ubiquitous phenomenon of metasomatism in the diagenetic realm (Warren, 2000; Machel, 2004), where carbonate rock (CaCO_3) interacts with magnesium-rich fluids to form dolomite [$\text{CaMg}(\text{CO}_3)_2$]. There are two main methods of dolomitization. The first relates to early dolomitization, that occurs at low temperature, and is related to: (i) bacterial activity early after deposition (Slaughter & Hill, 1991); (ii) specific chemical fluid conditions (Montes-Hernandez *et al.*, 2020); (iii) Mg supersaturation in seawater due to evaporation (reflux mechanism) (Nader *et al.*, 2012); or (iv) melange with continental water (Wilson *et al.*, 1990; Gasparrini *et al.*, 2006; Nader *et al.*, 2012). For all of the cases presented above, replacement involves constant renewal by Mg-rich water. The second category relates to late dolomitization, occurring in relation with an influx of ascending hydrothermal, Mg-heavy evolved fluids that flow and interact with carbonates during tectonism (Swennen *et al.*, 2012; Martín-Martín *et al.*, 2015; Mozafari *et al.*, 2019). The latter is usually referred to as hydrothermal dolomite regardless of the fluid origin (Machel & Lonnee, 2002), and is of important economic interest (Wallace *et al.*, 1994; Diehl *et al.*, 2010), namely because of a genetic link with base metal deposits (Gomez-Rivas *et al.*, 2014; Kelka *et al.*, 2015; Martín-Martín *et al.*, 2015; Kelka *et al.*, 2017).

To date, the large-scale dolomitization process is still under debate, with remaining questions about the source of fluids and its Mg content (Whitaker *et al.*, 2004; Gomez-Rivas *et al.*, 2014; Koeshidayatullah *et al.*, 2020b) on the pathways allowing for long-term renewed fluid migrations in tectonic context (Machel & Mountjoy, 1986; Whitaker *et al.*, 2004; Breesch *et al.*, 2010; Beaudoin *et al.*, 2014; Gomez-Rivas *et al.*, 2014; Chen *et al.*, 2016; Pinto *et al.*, 2017; Scribano

et al., 2017; Debure *et al.*, 2019; Quesnel *et al.*, 2019), and on the fluid transport limitation of the phenomenon at either outcrop-scale (Koeshidayatullah *et al.*, 2020b) or crystal-scale (Putnis & Putnis, 2007; Merino & Canals, 2011; Kondratiuk *et al.*, 2015). At the crystal-scale, two conceptual models compete to account for dolomitization: the growth-driven pressure-solution (Merino & Canals, 2011); and the dissolution–precipitation mechanism (Putnis & Putnis, 2007). Dolomite growth-driven pressure solution postulates a Mg-rich/Ca-poor solution that is undersaturated with respect to calcite. This model involves brine infiltration into the limestone, dissolving calcite and supersaturating itself with dolomite. During growth, the same volume of dissolved calcite becomes occupied by dolomite and turns out to be self-accelerating. Dissolution of calcite is controlled by fluid pressure becoming locally higher than the lithostatic pressure and implies a conservation of the solid volume (Merino & Canals, 2011). Dissolution–precipitation relies on the development of an interconnected porosity allowing the reaction to progress through the crystal/rock. Replacement occurs along the fluid–rock interface and the element exchange is maintained while supplies last (Putnis *et al.*, 2005; Raufaste *et al.*, 2011).

Several experimental studies on calcite/dolomite replacement suggested that the mechanism of dissolution–precipitation is more likely to happen than growth-driven pressure-solution (Machel, 2004; Putnis & Putnis, 2007; Jonas *et al.*, 2015, 2017; Kondratiuk *et al.*, 2015). This observation is also supported by experimental studies of different systems that are similar to dolomitization (Putnis & Mezger, 2004; Raufaste *et al.*, 2011; Kar *et al.*, 2015; Jonas *et al.*, 2017; Beaudoin *et al.*, 2018; Pedrosa *et al.*, 2016a,b). A direct assessment of such processes occurring in natural dolomite is still lacking.

Studies of trace elements in dolomite crystals can bring more details about the processes governing the reaction since they are very sensitive to fluid–rock interaction (see chapter 7 in White, 2013). Indeed, the incorporation of trace elements in carbonate minerals might result from a substitution between trace elements, Ca and probably Mg (Abele *et al.*, 1962; Welte, 1962; Deininger, 1964). Consequently, the rare earth element pattern (REE) can help to constrain; for example, the source of fluids involved in diagenesis (Haskin & Gehl, 1962; Piper, 1974; Henderson, 1984) and the redox condition of

dolomitizing fluids (Huang *et al.*, 2011; Zhou *et al.*, 2012; Ling *et al.*, 2013; Zhang *et al.*, 2014; Chen *et al.*, 2015).

While dolomitization interfaces are studied at the metre scale to examine the origin and large-scale migration mechanisms of dolomitizing fluids (Mozafari *et al.*, 2019; Koeshidayatullah *et al.*, 2020a), a detailed study of microstructural and chemical patterns at the scale of a natural limestone partially replaced by dolomite has never been reported. Yet, this study can validate insights from experiments and can suggest governing mechanisms of fluid transport at a small scale that undoubtedly impacts the larger-scale expression of the dolomitization. This study reports an analytical and textural study of a natural replacement front comprised of both original calcite and transformed dolomite from the Layens anticline, located in the north Pyrenean foreland (France). Based on X-ray microtomography (X-ray μ CT), scanning electron microscopy (SEM) and electron back scattered diffraction (EBSD), it is possible to quantify phase

proportions across the calcite–dolomite transition, and to see where dolomite is located in the rock (in three-dimensions) to characterize which mechanism is associated with the dolomitization reaction. The extent of mass transport has been determined to understand mass redistribution across the calcite–dolomite transition using an electron probe micro-analyzer (EPMA), femto laser ablation inductively coupled plasma mass spectrometry (fs-ICP-MS) and laser ablation ICP-MS (LA-ICP-MS), X-ray μ CT and mass balance equations. All of this led to establishment of the steps that affected the rock at crystal-scale during dolomitization, with special emphasis on transport mode, fluid pathways and chemical exchanges between the fluid and rock.

GEOLOGICAL SETTING

Preserved dolomitization fronts were recognized in the Layens anticline, located in the northern Pyrenean zone (Fig. 1). This anticline is part of

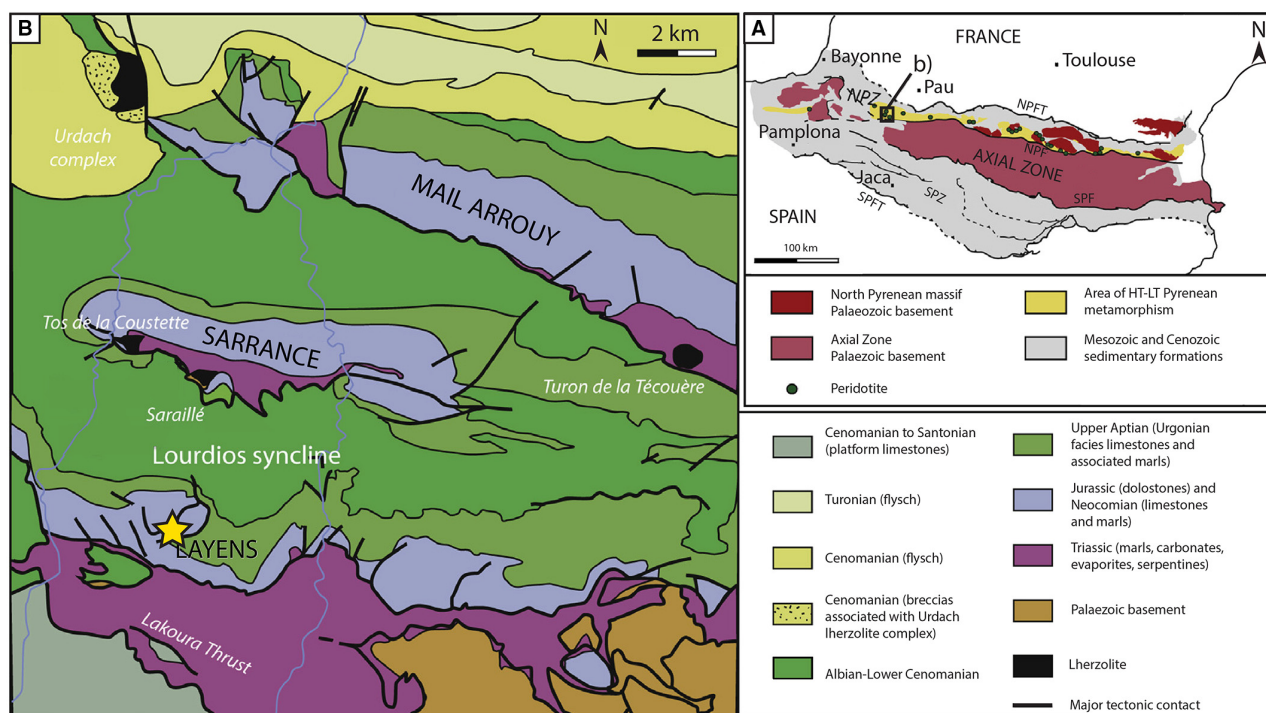


Fig. 1. (A) Structural map of the Pyrenees. NPFT: North Pyrenean Frontal Thrust, NPF: North Pyrenean Fault, SPF: South Pyrenean Fault, SPFT: South Pyrenean Frontal Thrust, NPZ and SPZ: North and South Pyrenean Zone, HP LT: High pressure low temperature (after Vacherat *et al.*, 2014). (B) Structural map of the Chaînons Béarnais region, with location of the panoramic view shown in Fig. 2 and of the map in Fig. 3 (rectangle) (modified after Castéras *et al.*, 1970; Lagabrielle *et al.*, 2010; Corre *et al.*, 2016). Location of the outcrop in this study shown by a yellow star (43°01'11.9"N, 0°39'15.3"W).

the Chaînons Béarnais, a sequence of three overturned anticlines with an east–west strike parallel to the Pyrenees chain (Labaume & Teixell, 2020). From the Triassic to the Jurassic, the opening of the Atlantic Ocean might have developed a normal fault network (Puigdefàbregas & Souquet, 1986). An extensional event started in the early Cretaceous with the formation of a rift (Tugend *et al.*, 2015; Teixell *et al.*, 2016). During this period of extension, the depocentres were affected by major faulting, developing tilted blocks at both kilometre and metre scales, leading eventually to the formation of one or several detachment faults that caused mantle exhumation (Lagabrielle *et al.*, 2010; Masini *et al.*, 2014). At the same time, the sedimentary succession was deformed and folded by the formation of salt diapirs (Triassic), including the Layens area (Izquierdo-Llavall *et al.*, 2020; Labaume & Teixell, 2020). This period was followed by a compressive event and a continental collision which started in the late Santonian (*ca* 80 Ma) and culminated in the middle Tertiary forming the present day antiformal stack of the Pyrenean belt (Mouthereau *et al.*, 2014; Teixell *et al.*, 2016).

Stratigraphy of the Layens anticline is extensively documented elsewhere (Lenoble, 1992; James, 1998). The sedimentary column starts with evaporites and marls (Keuper Marls, Upper Triassic), overlaid by interbedded marls and limestones (Aussurucq Limestones, Lias), partially dolomitized bioclastic limestone (Meillon Formation, Callovian–Oxfordian) and argillaceous limestones (Lons Limestones, Oxfordian–Kimmeridgian). This sequence is overlain unconformably by reef limestones (Lenoble, 1992). Published palaeofluid characterization relates the regional dolomitization of the Meillon Formation to a flow of hydrothermal magmatic fluids that became hypersaline in contact with Triassic evaporites, ascending along faults (Salardon *et al.*, 2017). The dolomitization event is synchronous with Albian–Cenomanian rifting and associated crustal thinning (Salardon *et al.*, 2017; Incerpi *et al.*, 2020), with a geothermal gradient around *ca* 80°C per kilometre (Vacherat *et al.*, 2014).

The studied calcite–dolomite interface was sampled in the Meillon Formation (43°01'11.9"N, 0°39'15.3"W). The distribution of the dolomite documented in the Meillon Formation cropping out in the Layens anticline is bound to the distribution of normal faults, but the contacts between dolostone and limestone are easily visible in the

field (Figs 2A, 2B and S1). Most of the contacts are marked by the presence of pressure-solution figures (i.e. stylolites) and the absence of a gradient between the host limestone and the newly formed dolomite (Fig. 2B).

ANALYTICAL METHODS

Sample description and preparation

Hand specimens of transition zones between the limestone and dolostone were collected in the field, and those exhibiting the wider and more gradual transition zone at their surface were selected for further investigations (Appendix S1). Because samples display a transition zone affected by pressure-solution, *in situ* analysis focussed on a single sample that exhibited the most preserved, complete record of the interface (Fig. 2C). Three polished thin sections (60 × 45 mm) were prepared across the entire hand specimen from the original calcite to the dolomite domain. Petrological characterization under optical microscopy (Nikon Eclipse LV100ND; Nikon, Tokyo, Japan) was carried out at the Laboratory of Complex Fluids and their Reservoirs (LFCR) at the University of Pau and Pays de l'Adour, (UPPA) Pau, France.

Phase characterization and distribution using X-ray tomography

A 3D quantitative characterization of the morphology and distribution of elements forming the rock was performed using X-ray computed microtomography (μCT). This technique was employed to quantify the local modal abundance of mineral phases across the replacement front. Four cores, 4 mm in diameter and 1.3 cm long were drilled, corresponding to the different zones observed across the hand specimen. The μCT scans were acquired on a Zeiss Xradia Versa 510 (Zeiss, Oberkochen, Germany) located at the Experimental X-Ray Methodology Development (DMEX, UPPA). To ensure an optimal voxel size, each core was scanned in four parts, and then the parts were stitched together. The resulting datasets, hereinafter referred to as scans, cover the full sample heights. All scans were acquired at a voltage of 80 keV and a power of 7 W with a magnification resulting in a pixel size of 2.65 μm (corresponding to voxel of 18.61 μm³, scans 1, 3 and 4) and 3.75 μm (voxel size of 52.73 μm³, scan 2). The core in scan 2 consists of coarser grains so

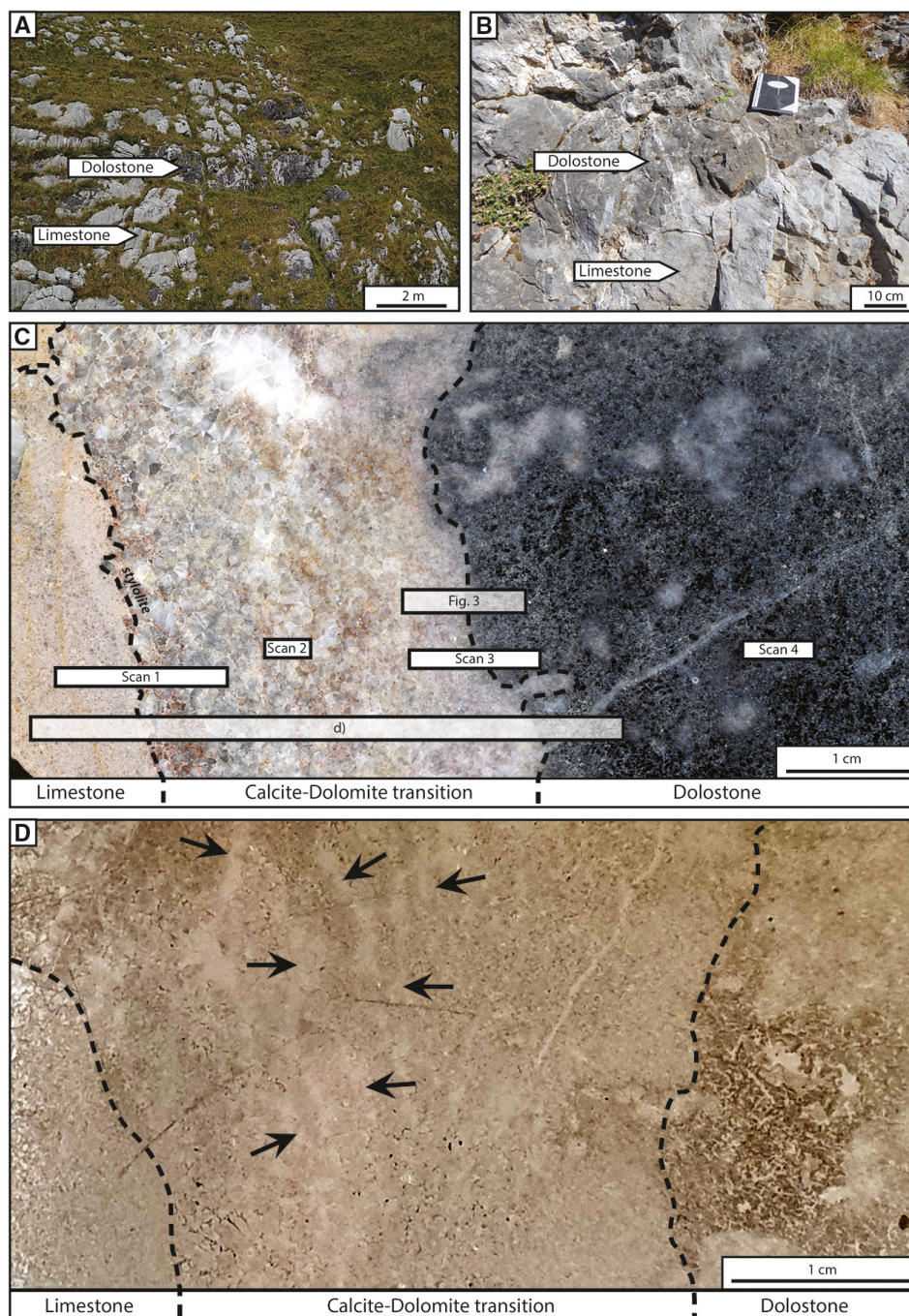


Fig. 2. (A) and (B) Photograph of the Callovian–Oxfordian limestone of the Meillon Formation cropping out in the Layens anticline. (C) High-resolution two-dimensional scan of a polished slab of studied calcite–dolomite interface. (D) Photograph of a coated thin section from across the hand specimen with location of lighter stripes (black arrows).

it has a $3.75\ \mu\text{m}$ pixel size; some spatial resolution was sacrificed to keep the scanning time within a reasonable time frame for this sample. This sample attenuated X-rays more strongly, possibly due to a local variation in porosity and

density. A total of 1601 projections were taken for each scan. The same exposure times were adjusted for each core (between 5.5 s, 8 s and 10 s) to maximize the signal to noise ratio. Volumes were reconstructed using a standard filtered

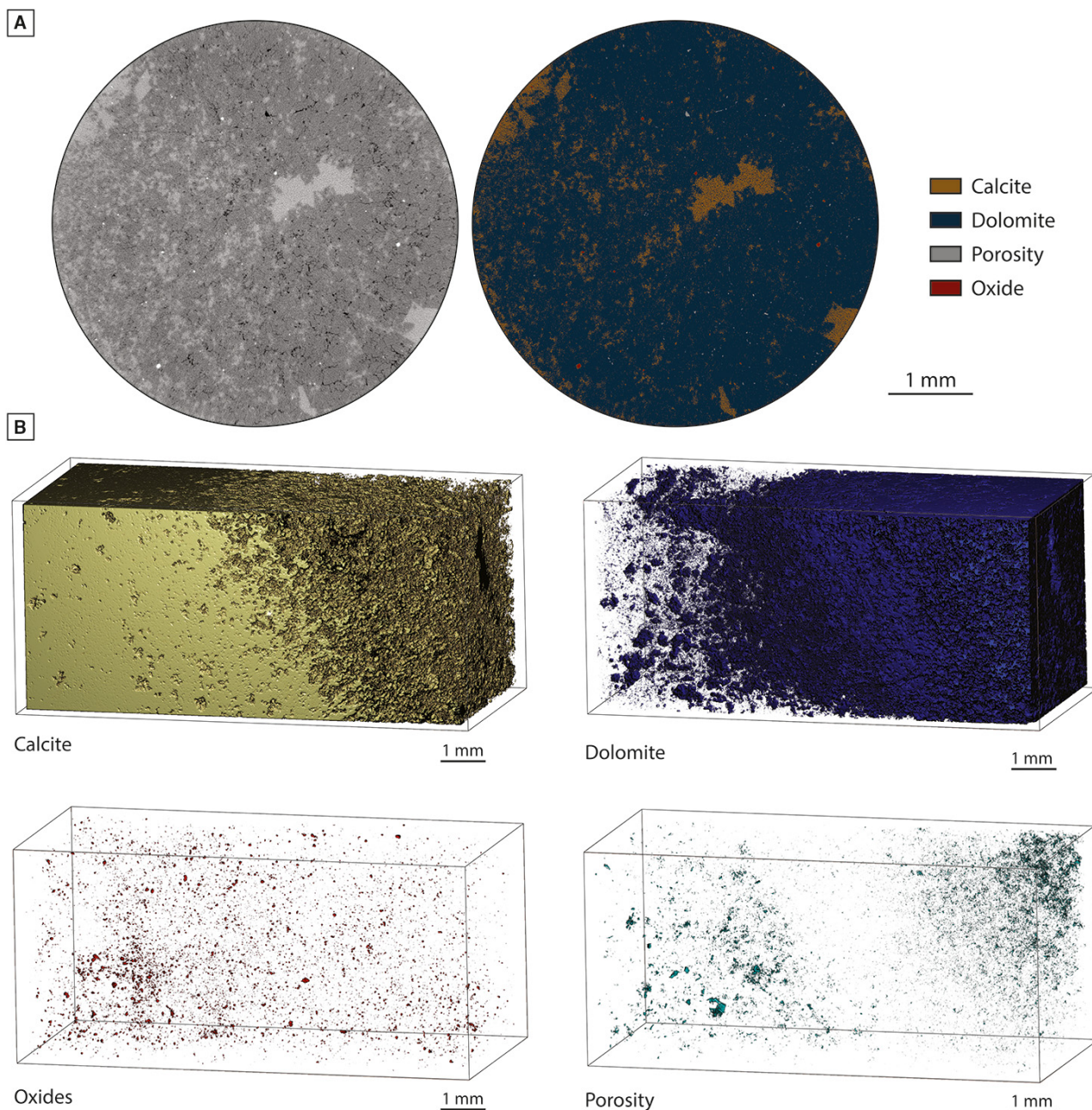


Fig. 3. (A) X-ray microtomography (μ CT) slice from the area of scan 3 with its phase segmentation based on the grey value of each voxel (which depends on its atomic number and density). (B) Three-dimensional volumes extracted from X-ray microtomography scan of scan 3 as located in Fig. 2. Each block represents one of the four constitutive phases of the rock.

back projection reconstruction algorithm (Ramachandran & Lakshminarayanan, 1971; Feldkamp *et al.*, 1984). Image processing was carried out with the proprietary image analysis software Dragonfly v.3.6.1.492, © 2020 Object Research Systems (ORS) Inc. The remaining noise was filtered using a median filter (Kernel size 3). The

data were manually segmented into four phases based on their greyscale values after BSE (backscattered electron) and EPMA (electron probe microanalyzer) control (Fig. 3). The greyscale values reflect the X-ray attenuation, which is function of a combination of the mean atomic number and density of the target material in

function of the polychromatic X-ray spectrum. The post-processing quantification of all of the features characterized, neglect anything smaller than 5 voxels, so less than $93\ \mu\text{m}^3$ for a pixel size of $2.65\ \mu\text{m}$ (or a voxel of $18.61\ \mu\text{m}^3$) and less than $263\ \mu\text{m}^3$ for a pixel size of $3.75\ \mu\text{m}$ (or a voxel of $52.73\ \mu\text{m}^3$). The volume selected to extract the phase proportions was $1\ \text{mm}^3$ to avoid overestimating the porosity and oxide fractions. This volume is at least two orders of magnitude higher than the biggest pore and the maximum grain size of oxides. The uncertainties on the phase proportion have been estimated by variation of threshold and by adding/removing a one-voxel thick layer on every cluster of voxels. The variation on phase proportion before and after the tow operations corresponds to the uncertainties.

Crystallographic analysis

Electron backscatter diffraction (EBSD) analysis was carried out at the Centre de MicroCaractérisation Raimond Castaing, Toulouse, using a JEOL JSM-7100TTLS LV (JEOL Limited, Tokyo, Japan). Electron backscatter diffraction data were acquired using an Oxford Instruments Aztec 3.4 EBSD and energy-dispersive X-ray spectroscopy (EDS) system (Oxford Instruments, Abingdon, UK) using an accelerating voltage of 20 keV and a beam size of $10\ \mu\text{m}$. Post-processing of EBSD data was done using HKL Oxford© Instruments Channel 5 v.5.12.72.0 software. A replacement of single pixels that were different (by some misorientation) from six nearest neighbours was applied. The change in the lattice parameters between calcite and dolomite due to band shifts make the phase separation difficult. Energy-dispersive X-ray spectroscopy mapping was used to separate calcite and dolomite with respect to $\text{Mg}/\text{Ca} > 1$ for dolomite and $\text{Mg}/\text{Ca} < 1$ for calcite (Pearce *et al.*, 2013).

Major elementary content

Major element compositions of calcite and dolomite were obtained using a JEOL JXA-8200 superprobe at the Institute of Geological Sciences, University of Bern (Switzerland). Analytical conditions were 1.5 nA beam current and 15 keV accelerative voltage and a beam size of $10\ \mu\text{m}$ to ensure stability of the material during the analysis. Calibration was performed using the CITZAF routine (quantitative matrix

correction) with natural and synthetic standards: dolomite (Mg), calcite (Ca), tephroite (Mn) and siderite (Fe).

Trace element concentration

Trace element data were collected using two different laser ablation setups. The first one was a Resonetics RESolutionSE 193 nm excimer laser system (Resonetics, Nashua, NH, USA) equipped with a S-155 large volume constant geometry chamber (Laurin Technic, Australia) at the Institute of Geological Sciences, University of Bern (Switzerland). The laser system was coupled to an Agilent 7900 quadrupole ICP-MS instrument (Agilent Scientific Instruments, Santa Clara, CA, USA). Samples were ablated in a He atmosphere and the aerosol was mixed with Ar carrier gas before being transported to the ICP-MS. The ICP-MS was tuned for low oxide production ($\text{ThO}/\text{Th} < 0.2\%$) and Th/U ratio close to one. Laser spots were ablated at 5 Hz using an $80\ \mu\text{m}$ beam diameter and a flux of $5\ \text{J cm}^{-2}$. The analyzed surface was cleaned by pre-ablation by three laser pulses employing a larger spot size. The total acquisition time for each analysis was 70 s, consisting of 30 s of gas background acquired with the laser switched off, 10 s of washout after pre-ablation cleaning and 30 s of ablation signal. Dwell times were 8 ms for ^{23}Na , ^{24}Mg , ^{44}Ca , ^{27}Al and ^{39}K ; 20 ms for rare earth elements (REE), ^{208}Pb and ^{238}U ; and 10 ms for ^7Li , ^9Be , ^{11}B , ^{45}Sc , ^{49}Ti , ^{51}V , ^{53}Cr , $^{54-55-56}\text{Fe}$, ^{55}Mn , ^{61}Ni , ^{66}Zn , ^{75}As , ^{85}Rb , ^{88}Sr , ^{89}Y , ^{111}Cd , ^{133}Cs , ^{137}Ba and ^{232}Th . External calibration was performed using trace element doped basaltic glasses GSD-1g (Jochum *et al.*, 2010) and NIST 612 (Jochum *et al.*, 2011) from the USGS, employing the preferred values listed in Peters & Pettke (2017), and ^{44}Ca and ^{24}Mg as internal standards (for calcite and dolomite, respectively). The concentrations obtained by EPMA were used for the calibration of LA-ICP-MS data. Data were reduced by employing Iolite (Paton *et al.*, 2011).

The second setup consisted of a femtosecond laser ablation system (Lambda3; Nexeya, Bordeaux, France) coupled to a high resolution ICP-MS (HR-ICP-MS) Element XR fitted with the Jet Interface (fsLA/HR-ICP-MS) (Thermo Fisher Scientific, Waltham, MA, USA). The laser is fitted with a diode-pumped Yb:KGW crystal laser source (HP2, Amplitude Systèmes, Pessac, France). Pulse duration is less than 400 fs at 257 nm. The laser source can operate within a wide range of

repetition rates (1 Hz to 100 kHz) and energy ranging from 200 μJ per pulse below 1 kHz to 1 μJ at 100 kHz at 257 nm. Complex trajectories can be realized by moving the laser beam (15 μm diameter at full energy) across the surface of the sample using the rapid movement of galvanometric scanners combined with a high repetition rate (Aramendía *et al.*, 2015; Donard *et al.*, 2017).

The aerosol produced by the ablation was carried to the ICP-MS by a tube (1/16" internal diameter) using a He stream (600 mL min^{-1}) leading to a measured wash out time of the ablation cell of *ca* 500 ms: 10 mL min^{-1} of nitrogen was added to the He flow before mixing with argon in the ICP-MS in order to improve the signal sensitivity. Measurements were performed under dry plasma conditions. The fsLA-ICP-MS coupling was tuned on a daily basis in order to achieve the best compromise in terms of sensitivity, accuracy, particle atomization efficiency and stability. The additional Ar carrier gas flow rate, torch position and power were adjusted so that the U/Th ratio was close to 1 ± 0.05 when ablating the glass SRM NIST612. NIST612 and NIST610 were used for calibration standards and ^{43}Ca was used as internal standard (Jochum *et al.*, 2011). Detector cross-calibration and mass bias calibration were checked daily using the appropriate sequence of the Element Software. ^{25}Mg , ^{35}Cl , ^{43}Ca , ^{51}V , ^{66}Zn , ^{85}Rb , ^{88}Sr , ^{89}Y , ^{139}La , ^{140}Ce , ^{141}Pr , ^{146}Nd , ^{150}Sm , ^{153}Eu , ^{158}Gd , ^{159}Tb , ^{163}Dy , ^{165}Ho , ^{166}Er , ^{169}Tm , ^{172}Yb , ^{175}Lu , ^{208}Pb and ^{238}U were selected in low resolution mode ($R = 300$) with a dwell time of 30 ms.

Images were built from the fsLA/HR-ICP-MS signal resulting from the sample's ablation according to a series of horizontal lines vertically distributed with 20 μm spacing (centre to centre). Taking into account that the washout time of the laser cell (based on 99% criterion) was about 0.5 s and the ICP-MS was set to acquire 0.84 points per second, the sample translation was set to 9 $\mu\text{m s}^{-1}$ and the space between lines was set to 20 μm in order to obtain square pixels of $20 \times 20 \mu\text{m}$. In other words, the image resolution was set to 20 μm . In these conditions the signal corresponding to $5.2 \times 2.2 \text{ mm}$ was acquired in 9.5 h.

RESULTS

Petrology

The studied specimen is characterized by three main parts: (i) the original (non-reacted) rock

consisting of small-sized (<millimetre) crystalline calcite (Fig. 2C, left-hand side); (ii) a calcite–dolomite transition consisting of *ca* 2.5 cm of coarse calcite (millimetre) and *ca* 0.5 cm of fine calcite (<millimetre) (Fig. 2C, centre); (iii) the replaced rock consists of small-size (<millimetre) non-pervasive euhedral crystals of dolomite. A pressure-solution zone, marked by stylolites, separates the calcite domain (dashed line on the left, Fig. 2C). Strikingly, contacts between the three parts described before are parallel to one another (dashed lines, Fig. 2C). In the calcite–dolomite transition part, a zebra-like alternation of darker and lighter calcite stripes appears oriented parallel to the contact with the calcite (Fig. 2D and E).

Phase characterization and distribution

Three mineral phases plus the porosity were segmented by μCT based on distinct ranges of grey values (Fig. 3), in line with the results of the SEM-EDS-EPMA analysis (Fig. 4). The following progression goes from the lower range of grey values to the highest: porosity, dolomite, calcite and oxides. Dolomite appears darker than calcite on the μCT volumes suggesting the presence of an intragranular porosity within dolomite below the threshold of resolution of μCT (Fig. 4).

The integration of EBSD data with the volume fraction obtained by μCT allowed to define four zones across the sample (Fig. 5).

1 Original calcite. Grains exhibit a constant size around 100 μm in diameter, a low porosity (0.5 to 1.0 vol.%) and oxides located along the grain boundaries (Fig. 4A). Stylolites are present at the contact with the calcite–dolomite transition.

2 Reaction zone A. Calcite grains are larger, between 200 μm and 1.5 mm in diameter, with a low porosity (<0.5 vol.%) and some oxide inclusions. Oxides and porosity are located along the grain boundary network (Fig. 4B). All oxides represent *ca* 0.1 vol.%. Dolomite is present at grain boundaries (<1 vol.%).

3 Reaction zone B. This zone is depleted in calcite and enriched in dolomite compared to zone A. The porosity is higher (>0.5 vol.%) and appears within calcite and dolomite grains and along grain boundaries (Fig. 4B to D). The grain size of calcite decreases from 300 μm to less than 50 μm across zone B towards the dolomite

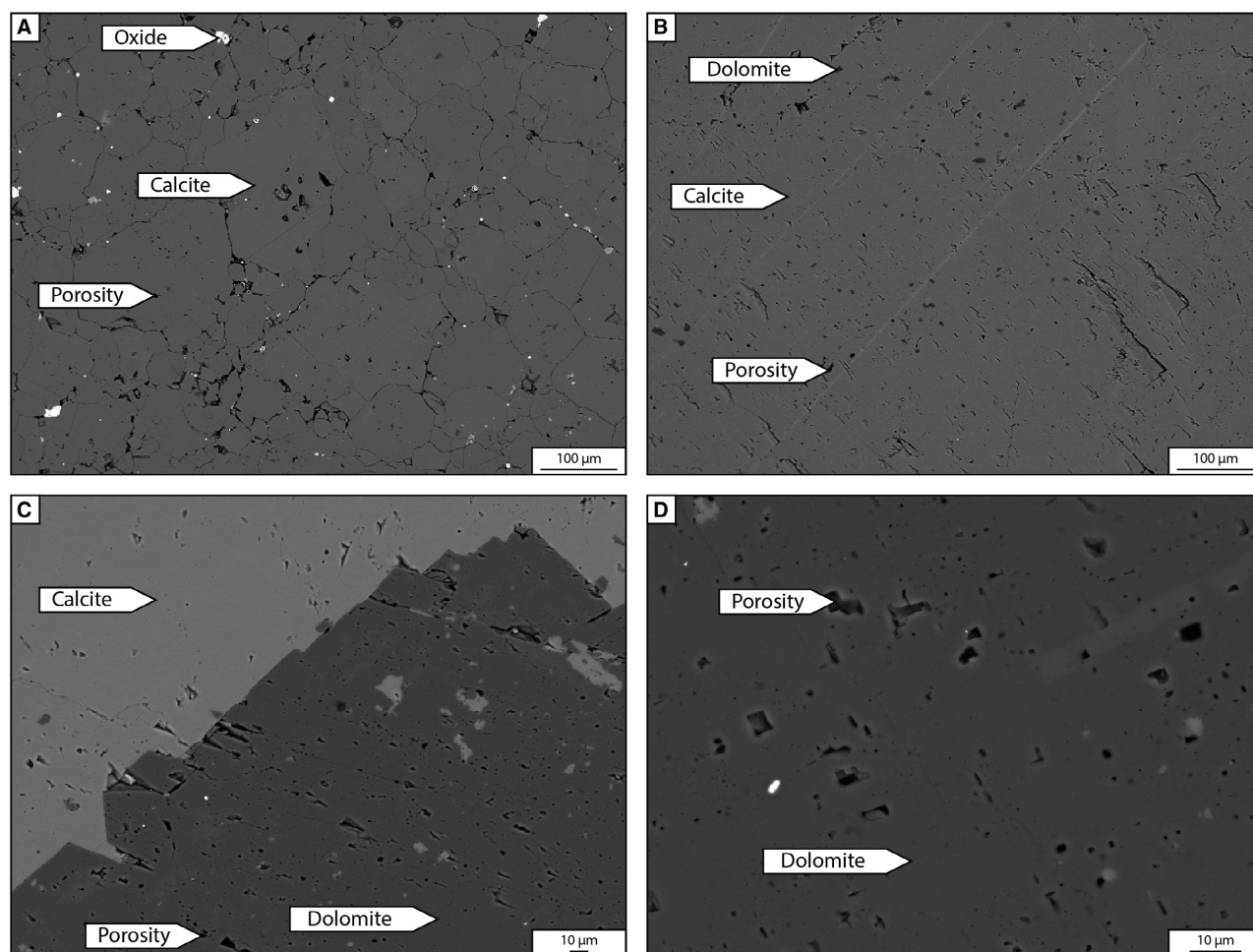


Fig. 4. Scanning electron microscopy (SEM) backscattered images of the sample showing: (A) the general aspect of the original calcite; (B) calcite in reaction zone; (C) and (D) dolomite.

on the right. Oxide abundance is higher when compared to zone A (*ca* 0.7 vol.%).

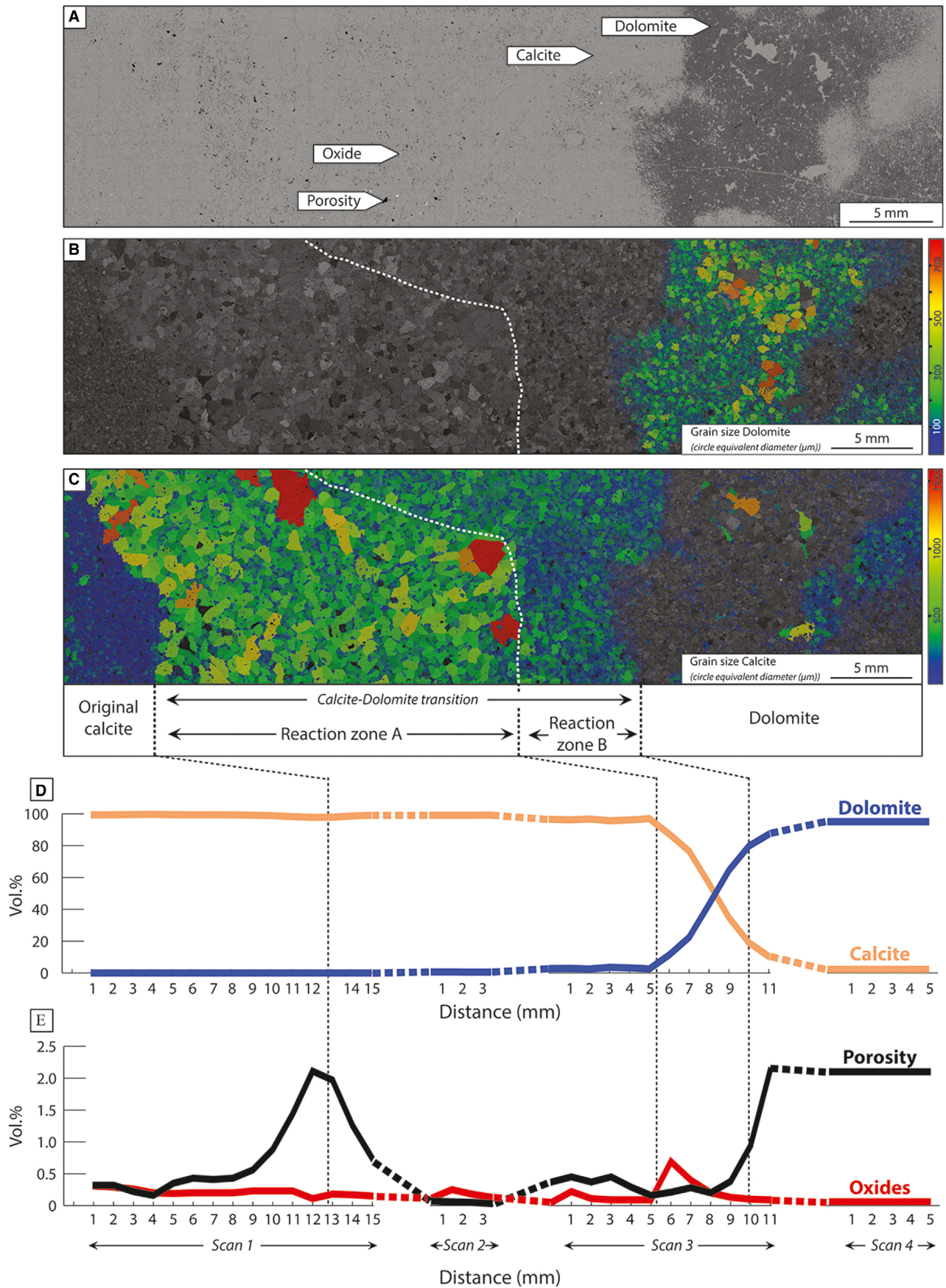
4 Dolomite domain. This domain exhibits a progressive increase in crystal size away from reaction zone B. Porosity and oxides contents are constant throughout the domain (*ca* 2 vol.% and *ca* 0.1 vol.%, respectively).

Neither calcite nor dolomite shows a crystallographic preferred orientation in the subsets of *ca* 5 mm² across the sample (Fig. S2). The volume of porosity is constant across the four

zones within the analytical uncertainties. The grain size of calcite and dolomite change gradually in opposition from reaction zone A to the dolomite domain (Fig. S3). The uncertainties on the phase proportion (by variation of threshold and by adding one layer of voxel) is around 14 vol.% for the dominant phase (calcite and dolomite) and less than 1 vol.% for the oxides and the porosity.

The 3D distribution of dolomite and porosity in reaction zone A is shown in Fig. 6A. The

Fig. 5. (A) Backscattered electron (BSE) image of the calcite–dolomite transition. Dolomite (B) and calcite (C) grain size overlain in semi-transparency with band contrast (circle equivalent diameter in µm). Band contrast represents the electron backscatter pattern quality, the brighter the value, the better the diffraction quality. Volume percent profile of calcite–dolomite (D) and porosity–oxide (E) segmented from the X-ray CT scan calculated in subvolumes of around 1 mm³. X-axis represents the length and position of each core. Scan location is shown in Fig. 2C.



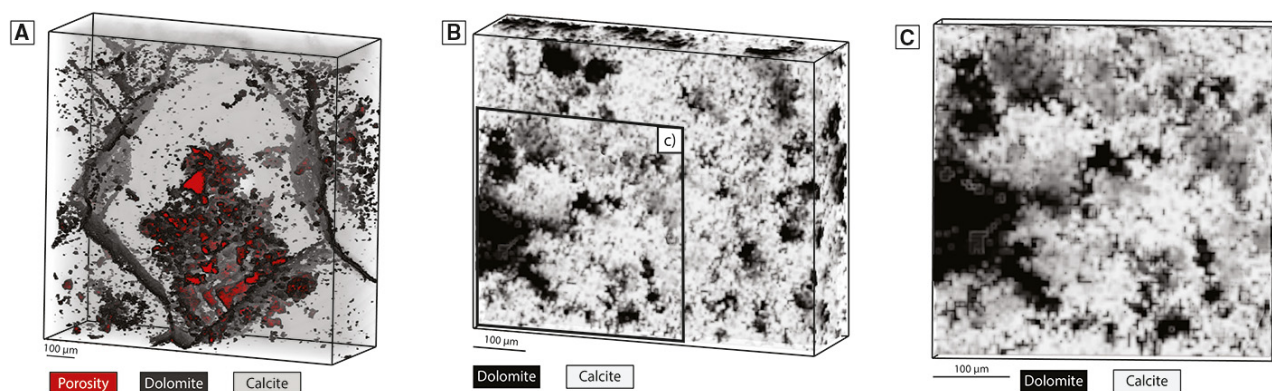


Fig. 6. (A) Three-dimensional volume in reaction zone A of the coarse calcite showing the replacement of calcite (light transparent white) by dolomite (black) and porosity (red). (B) 3D volume in reaction zone B of the coarse calcite showing the replacement of calcite (light grey) by dolomite (black). Note the small-scale infiltration of dolomite in the calcite patches in (C).

calcite grains (low opacity) are partially dolomitized. Dolomite (in black) is associated with the porosity (red) in the grain boundary region and within the calcite grains. When the replacement is more advanced (for example, reaction zone B), the grains of calcite become more and more isolated from one another, and dolomite is distributed in the crystal in dendrite-like channels (Fig. 6B and C).

Mineral chemistry

The major element composition of both calcite and dolomite is uniform throughout the sample, with a composition close to pure calcite and pure dolomite (Table S1). In detail, original calcite Mg content ranges between 0.13 to 0.31 wt.%, with nearly no Mn or Fe (<0.03 wt.% in total). Magnesium content in calcite in the reaction zone ranges between 0 to 0.43 wt.% with nearly no Mn or Fe (less than 0.03 wt.%). Dolomite contains less than 0.1 wt.% Fe and Mn. Hematite is the only oxide detected in the hand specimen. The concentrations in trace elements are variable between the original calcite and the calcite located in the calcite–dolomite transition at 2 se (two standard errors, Fig. 7; Table S1). The REE pattern of original calcite is slightly negative, with a relative enrichment in heavy REEs (HREE: Tb to Lu) compared to light REEs (La to Gd). This important variation is due to the presence of small grains, porosity and small oxides (visible with in BSE) compared to the laser beam size (80 µm). Calcite in the reaction zone has a relatively flat REE pattern, with higher LREE content compared to the original

calcite. A positive Eu anomaly in the two calcites is present. Dolomite has a REE pattern comparable to that of the original calcite, although with slightly higher La, Ce, Pr and Nd concentration and slightly lower HREE content. A similar decrease in Tm content in calcite from the reaction zone is also observed. The major differences in trace element content are observed for U, Zn, Ba, Na, V, Cr and Sr (Table S2).

Trace element maps were collected in the calcite–dolomite transition zone A to visualize the redistribution of trace elements between calcite and dolomite and possible heterogeneities (Fig. 8). It corresponds to scan 2 used for X-ray µCT. Image segmentation was performed based on pixel densities using the Binary module of XMapTools 3.3.1 (Lanari *et al.*, 2014, 2019). The ‘mixed’ phase (Fig. 8A) corresponds to pixels with intermediate compositions between calcite and dolomite. The group containing these pixels is closer in composition to the dolomite (purple, Fig. 8). Oxides (red, Fig. 8A) are located at the grain boundaries of calcites and have the highest concentration of Zn and Pb (Fig. 8B and C).

INTERPRETATION

Origin of dolomitization

The regional dolomitization of the Meillon Formation could be related to an infill of hydrothermal hypersaline fluids flowing along faults related to Cretaceous rifting and

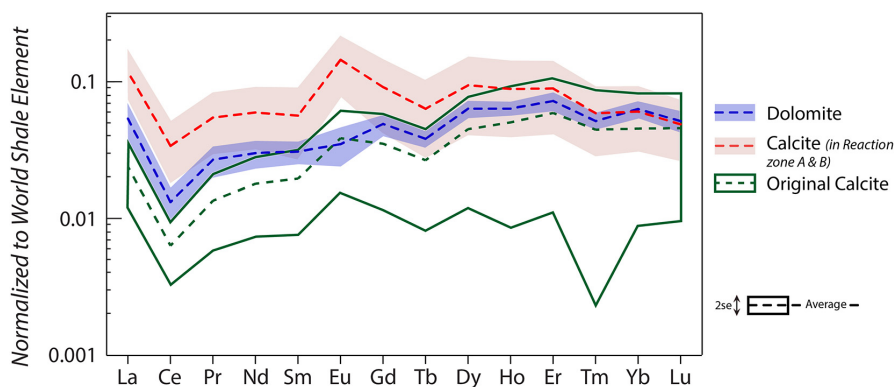


Fig. 7. Spider diagram for individual phases normalized to world shale (Piper, 1974). Each area represents all of the measurements at 2 se (standard error). The large range of values at 2 se is due to a small grain size associated with porosity and oxides present at grain boundaries.

associated with crustal thinning (Salardon *et al.*, 2017; Incerpi *et al.*, 2020), leading to a geothermal gradient of $ca\ 80^{\circ}\text{C km}^{-1}$ (Vacherat *et al.*, 2014). However, no fluid temperature data were collected in the Layens anticline because all observed fluid inclusions are below $5\ \mu\text{m}$. It is proposed that chemical and crystallographic patterns documented in the calcite–dolomite interface are an indirect validation of the hydrothermal origin of the dolomite of the Meillon Formation. Indeed, an alternation between lighter and darker stripes in thin section shown in Fig. 2D is similar to the zebra texture that is typical of base metal ore deposits (Zn–Pb) linked to hydrothermal dolomite formations (Leach & Viets, 1992; Wallace *et al.*, 1994; Krug *et al.*, 1996; Paradis *et al.*, 2007; Palinkaš *et al.*, 2009; Diehl *et al.*, 2010; Kelka *et al.*, 2015, 2017; Kelka, 2017). The zebra pattern indicates that the original calcite experienced recrystallization and coarsening prior to or during the early dolomitization stage. Such a recrystallization process can be related to either fluid pressure or stress waves linked to a first step of fluid infiltration, and/or to stress around fracture zones (Kelka *et al.*, 2015, 2017; Centrella *et al.*, 2018). Trace element maps (Fig. 8) show that, in the transition zones A and B, oxides and dolomite are located at grain boundaries, both with higher concentrations of Zn and Pb than in calcite (Fig. 8; Table S2). Additionally, redox conditions of dolomitization are obtained using trace elements such as Mn, V and U (Huang *et al.*, 2011; Zhou *et al.*, 2012; Ling *et al.*, 2013; Zhang *et al.*, 2014; Chen *et al.*, 2015). These three elements are more concentrated in dolomite, assuming a general reduced environment,

again similar to base metal ore deposits (Zhang *et al.*, 2014).

In the absence of available microthermometric data it is difficult to estimate the temperature formation of dolomite in order to confirm the hydrothermal fluid argument. This can be done using a succession of observations: the documentation anywhere else of proto-zebra-like patterns in poorly transformed calcite in a reduced environment coupled to higher concentrations of base metals in the dolomite precipitated at the grain boundaries suggests that the dolomitization of the Meillon Formation in the Layens is related to a hydrothermal fluid flow, likely linked to the magmatic fluid flow documented regionally (Salardon *et al.*, 2017).

Mass change during dolomitization

Mass balance calculations can be used to quantify element mobility during fluid-induced reactions (Ague, 1991; Centrella *et al.*, 2015, 2016, 2018; Centrella, 2019), but knowledge of local density and specific volume changes is required. Following Gresens (1967), the overall element gain/loss ratio during replacement of calcite by dolomite can be evaluated as function of the solid volume variation ($\Delta V_{\text{reaction}}$, Fig. 9A):

$$fv \left(\frac{g_{\text{Dol}}}{g_{\text{Cal}}} \right) \times c_n^{\text{Dol}} - c_n^{\text{Cal}} = x_n \quad (1)$$

With fv as the volume factor further converted to volume change ($\Delta V_{\text{reaction}}$). For example, a volume factor of 0.9 corresponds to 10% volume loss. The quantities g_{Dol} and g_{Cal} are the density

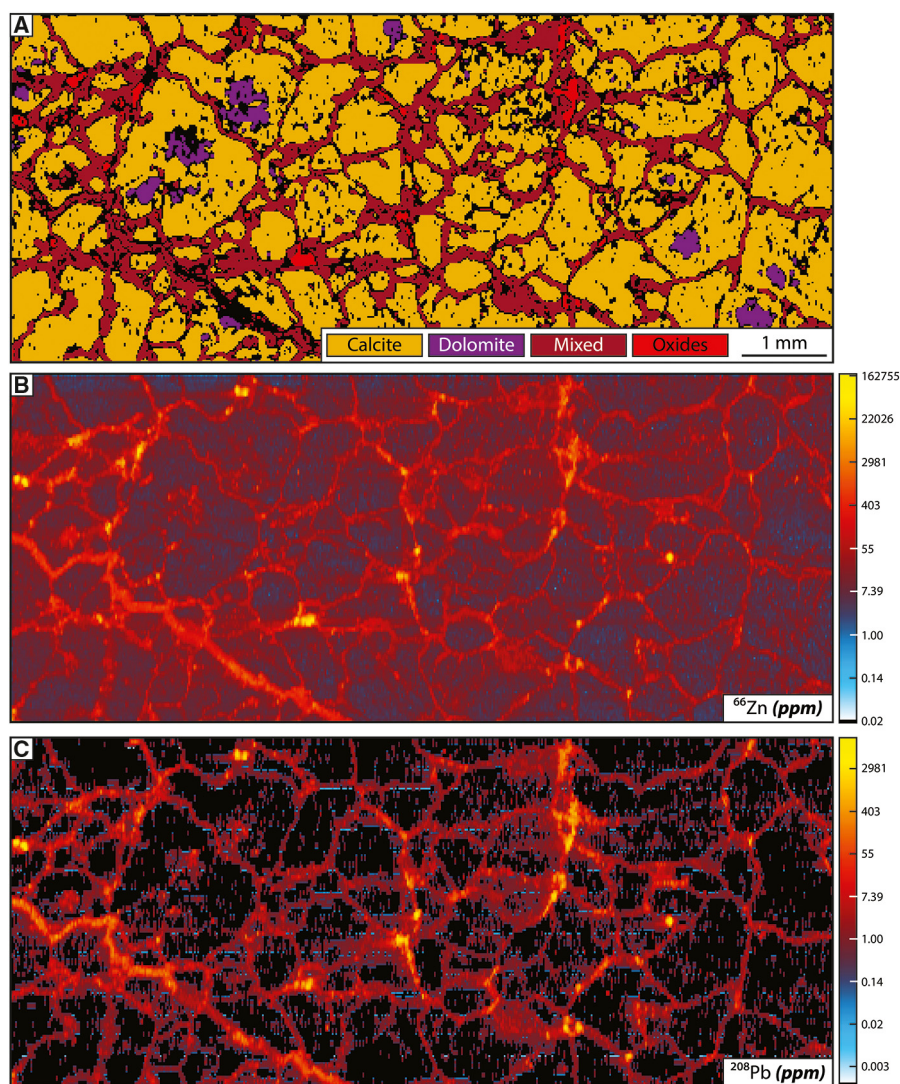


Fig. 8. Sample located in the calcite–dolomite transition (scan 2). Phase map (A) with associated Zn (B) and Pb (C). Maps were calibrated using Ca in calcite, the absolute concentration values are only valid for the pixels of calcite. Using Mg in dolomite as internal standard, the concentration of the mixed phase changes about one order of magnitude becoming closer to the dolomite concentration. Note that the colour scale is logarithmic. Pixel size $20 \times 20 \mu\text{m}$.

of dolomite and calcite, respectively, c_n^{Dol} and c_n^{Cal} the weight fractions of component n in minerals whereas x_n represents the gain or the loss for each component.

The selected average composition for the calcite is the one located in the reaction zone because dolomite is missing in the original calcite domain on the left side of the stylolite (Fig. 2). The average composition for the dolomite corresponds to the fully transformed zone for dolomite. Both minerals are close to the pure end-member compositions (oxide weight percentage, Table S1). Consequently, theoretical

values of 2.71 g cm^{-3} for g_{Dol} and 2.84 g cm^{-3} for g_{Cal} (Steinfink & Sans, 1959; Graf, 1961) can be used in Eq. 1. For the average calcite and dolomite composition, the weight fraction of CO_2 in calcite and dolomite was not measured with the analytical techniques employed. They were approached by a difference between the expected total oxide weight percent (i.e. 100 wt.%) and the sum of the values obtained for all measured elements (i.e. 53.35 wt.% for calcite and 49.82 wt.% for dolomite), giving dolomite $c_{\text{CO}_2}^{\text{Dol}}$ of 50.18 wt.% and calcite $c_{\text{CO}_2}^{\text{Cal}}$ of 46.65 wt.%. The $\Delta V_{\text{reaction}}$ can be approximated either by

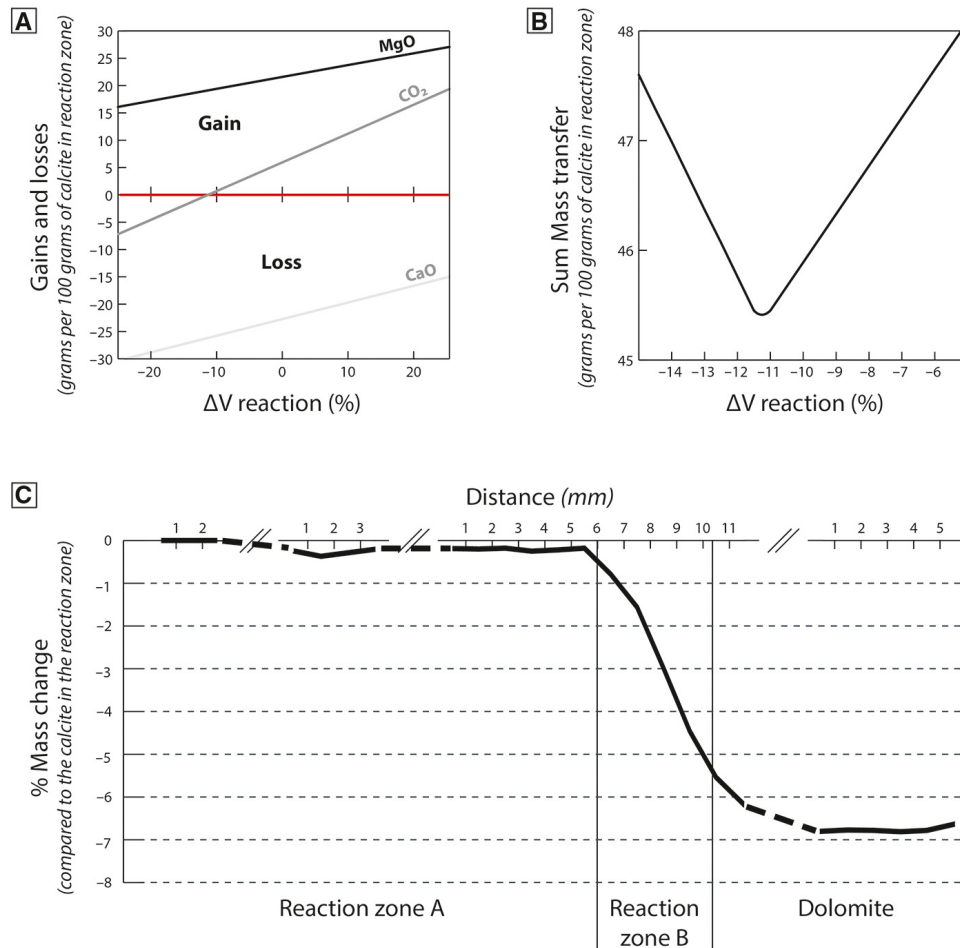


Fig. 9. (A) The overall gains and losses of elements from the replacement of calcite in a reaction zone by dolomite is plotted as a function of the volume change during the reaction. See text for details. For clarity, MnO and FeO are not shown. (B) Sum of gains and losses of elements as a function of the volume change during the reaction. (C) Profile of mass change (%) across the reaction zone taking into account the proportion of dolomite and calcite derived from X-ray μ CT (Fig. 4C). These proportions are coupled to the mass balance equation where the fully replaced calcite formed 93.13 g of dolomite (100 vol.%) and corresponds to *ca* 7% of mass loss and a $\Delta V = -11\%$.

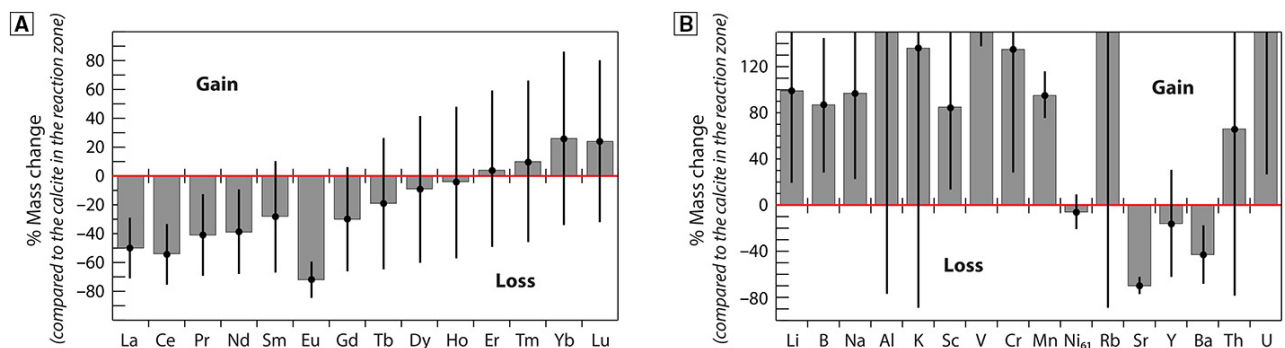
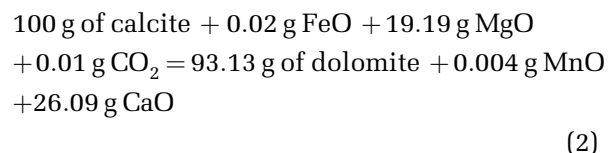


Fig. 10. Overall gains and losses of rare earth elements (REEs) (A), high field strength elements and large ion lithophile elements (HFSE – LILE) (B) during dolomitization with 11% of volume loss. Error bars represent the 2 se (standard error). For greater visibility, gain in mass is fixed at 100% (A) and 150% (B). Aluminium, V and U gained +207%, +259% and +693% of mass, respectively. Since these elements are present in low concentrations in calcite, a small variation in concentration results in a large variation in mass.

assuming one element to be immobile or by minimizing the flux of mass transfer (Hermann *et al.*, 2013). Since it is difficult to know for any reaction which element could be immobile (Ague, 1994), the second method of minimizing the mass transfer was favoured (Fig. 9B). This method sums the masses (elements) from the reactant and the product for different $\Delta V_{\text{reaction}}$ and selects the $\Delta V_{\text{reaction}}$ where the sum is the lowest. Calculations in this study show that for measured concentrations, the mass transfer occurring during replacement of calcite by dolomite is a minimum of a $\Delta V_{\text{reaction}}$ of *ca* -11%; i.e. the volume of solid is reduced by 11% (Fig. 9B). The effect of the uncertainty for both calcite and dolomite densities is negligible. If considering a variation of 5% and the $\Delta V_{\text{reaction}}$ change is less than 1%, these are neglected in the following discussion. Note that using pure end-member

calcite and dolomite compositions results in a slightly lower $\Delta V_{\text{reaction}}$ of -16%. This shows that the consideration of Fe and Mn in the mineral composition changes the $\Delta V_{\text{reaction}}$ by about 5% with respect to pure calcite and dolomite compositions. In terms of mass transfer, and still assuming a $\Delta V_{\text{reaction}}$ of -11%, the calcite to dolomite reaction can be written as follows:



In this model, only 93.13 g of dolomite is made from 100 g of original calcite, resulting in 7 wt.% of net mass loss that needs to be extracted by the fluid phase. Considering the respective phase proportion across the reaction

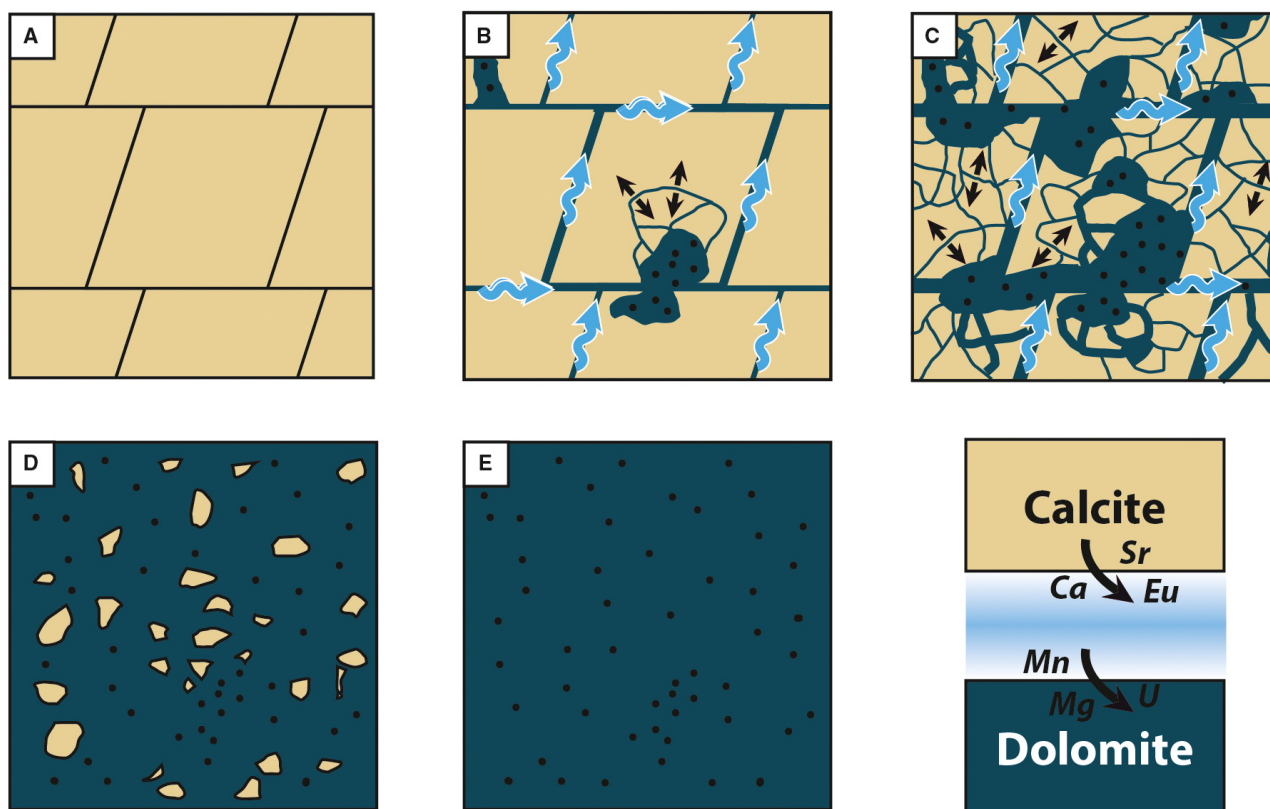


Fig. 11. Schematic sketch illustrating the entire replacement of calcite by dolomite. (A) Recrystallization of the original calcite into a coarse-grained calcite. (B) Fluid infiltration (blue arrows) through grain boundaries and dolomite precipitation. Fluid infiltrates some crystals and generates porosity. Element exchange between the fluid, calcite and dolomite is constant and shown in the lower right corner of the figure. (C) Fluid/dolomite continues to infiltrate the crystal and starts to isolate some calcite crystals. Replacement continues with isolated calcite crystals (D) still present until being fully replaced (E). Black dots represent the porosity and black arrows the diffusion limited replacement.

zones A and B and the mass balance (Eq. 2), a profile of mass change can be simulated (Fig. 9 C). In reaction zone A, the mass variation is not significant whereas in reaction zone B, the mass drops to reach *ca* 7% of mass loss.

Mass balance calculations can also be made with trace elements since the pattern between the calcite in the reaction zone and the dolomite (REE) is similar (Fig. 10A) (Centrella *et al.*, 2016; Ague, 2017). During dolomitization, LREE are fractionated rather than HREE. From La to Nd, *ca* 40% of mass is lost. Europium is the element that has been the most leached during dolomitization with 72% of mass loss. The average gain and loss of all REE gives 40% of mass loss during dolomitization of calcite. Other diagnostic trace elements are presented in Fig. 10B.

DISCUSSION: CONCEPTUAL MODEL FOR HYDROTHERMAL DOLOMITIZATION

Hydrothermal dolomitization is a multi-scale problem, with competing replacement models occurring at the crystal-scale [dissolution precipitation *sensu* Putnis & Putnis (2007), growth driven pressure solution *sensu* Merino & Canals (2011)] and conceptual models of large-scale fluid flow and recharges (Gomez-Rivas *et al.*, 2014; Mozafari *et al.*, 2019; Koeshidayatullah *et al.*, 2020a,b). The Meillon Formation in the Layens anticline, north Pyrenees, exhibits a rare occurrence of a sequence of partial replacement fossilized at the outcrop scale, giving an alternate and complementary view of published dolomitization front studies at the metre-scale, that deals with larger scale fluid dynamics (Koeshidayatullah *et al.*, 2020b). The steps of replacement are inferred from analytical, morphological and chemical analyses performed across the transition from calcite to dolomite. From the analyses of the two main reaction zones observed in the transition zone, a generic model with specific constraints over the factors and transport mechanisms that control elementary exchange between fluid and rock (Fig. 11) is proposed. Figure 11 illustrates the schematic replacement sequence starting by fluid infiltration in the host limestone, by advection channelized along grain boundaries (Fig. 11B). This type of replacement by advective transport is commonly evoked to explain the general wavy morphology of the replacement front (Fig. 2A) (Szymczak & Ladd, 2006, 2014; Kondratiuk *et al.*, 2015; Beaudoin

et al., 2018). The subsequent reaction with calcite grains seemingly involves calcite dissolution, as witnessed by identified micro-scale dendrite-like patterns (Fig. 6B and C), symptomatic of dissolution in granular media (Golfier *et al.*, 2002; Erikssen *et al.*, 2015; Xu *et al.*, 2018). It is proposed that the calcite is dissolved, releasing elements like Sr, Ca and LREE through the fluids, and is replaced simultaneously by dolomite, in a diffusion-limited process. This is an observation that is in accordance with experimental findings (Jonas *et al.*, 2015, 2017) and allows for the transfer of fluid transport and of dissolution–precipitation mechanisms from the experimental to natural diagenetic domain. As a function of how the system is open to mass transfer, localized stress can be generated during the reaction as a result of local density changes in the solid system (Wheeler, 1987; Ague, 1991, 1994; Jamtveit *et al.*, 2000, 2008; Jamtveit & Hammer, 2012; Kelemen & Hirth, 2012; Centrella *et al.*, 2015, 2016, 2018; Centrella, 2019). In the case of dolomite replacing calcite, density increases by about 5% (Steinfink & Sans, 1959; Graf, 1961) meaning that the volume of the solid phase decreases. If the overall volume stays constant, porosity is generated to compensate for the density increase. Multiple experiments show this porosity generation when a single phase is replaced by a denser one (Putnis, 2002; Putnis & Putnis, 2007; Ruiz-Agudo *et al.*, 2014; Pedrosa *et al.*, 2016a,b). The porosity is not only a consequence of a reduction in solid molar volume but dependent on the relative solubilities of parent and product solid phases in the reactive fluid. More of the parent material may be dissolved than the product reprecipitated, thus generating porosity. With the generated nanometre-scale to micron-scale porosity, dissolution–precipitation progresses in the crystal and isolated calcite islands from one another (reaction zone B, Fig. 11D and E), until the crystals are completely replaced by dolomite.

CONCLUSIONS

The preservation of a dolomitization front of the limestone of the Meillon Formation in the Layens anticline is remarkable and grants access to a fossilized sequence displaying the expression of gradual degrees of dolomitization. The detailed investigation of crystallographic and chemical patterns at the interface between the original limestone and the dolomite allows assessment of the hydrothermal origin of the

dolomitizing fluids in the Layens anticline. The first step of replacement is associated with Zn-Pb rich dolomite precipitation in a reduced environment, along the grain boundaries, triggering the development of zebra-like patterns. Crystal-scale patterns of distribution of dolomite when the replacement is more advanced suggest that the crystal-scale propagation of dolomitization is controlled by diffusion-limited dissolution–precipitation process.

Mass balance calculations coupled with elementary transfer show that hydrothermal dolomitization involves a net mass loss of *ca* 7 wt.% for major element and *ca* 40 wt.% of rare earth elements (REE) via aqueous fluid. This process is associated with the generation of porosity which compensates for the increase of density of dolomite crystals compared to calcite crystals. To account for the distribution patterns, it is proposed that this porosity generation is a key factor that allows the dissolution–precipitation to progress further in the crystal-scale as a self-enhanced mechanism, rather than using existing mineralogical defects. This study of a well-preserved natural case of a dolomitization front is a further step in suggesting that the propagation of dolomitizing fluids and the related front may be tied to crystal-scale reactive transport mechanisms. The unravelling of transport mechanisms and crystal-scale pathways is an important step towards a more realistic comprehension of hydrothermal dolomitization at a larger scale.

ACKNOWLEDGEMENTS

This work is funded by the project TXM-R2 (Institut Carnot ISiFOR), S.C. and N.B. are funded through the isite-E2S, supported by the ANR PIA and the Région Nouvelle-Aquitaine. We thank Pascale Sénéchale for all the μ CT scanning and volume reconstruction, Arnaud Proietti for the EBSD analyses and the help for the data processing. We thank Juan Diego Martín-Martín, three anonymous reviewers, and the Associate Editor Hairuo Qing for their interesting comments that improved the manuscript.

DATA AVAILABILITY STATEMENT

The data that support the findings of this study are openly available in Appendix S1 of the present study.

REFERENCES

- Abele, G., Berger, K. and Salger, M. (1962) Die Uranvorkommen im Bursandstein Mittelfrankens. *Geol. Bavarica*, **49**, 3–90.
- Ague, J.J. (1991) Evidence for major mass transfer and volume strain during regional metamorphism of pelites. *Geology*, **19**, 855–858.
- Ague, J.J. (1994) Mass transfer during Barrovian metamorphism of pelites, South-Central Connecticut. I: Evidence for changes in composition and volume. *Am. J. Sci.*, **294**, 989–1057.
- Ague, J.J. (2017) Element mobility during regional metamorphism in crustal and subduction zone environments with a focus on the rare earth elements (REE). *Am. Miner.*, **102**, 1796–1821.
- Ague, J.J. and Nicolescu, S. (2014) Carbon dioxide released from subduction zones by fluid-mediated reactions. *Nature Geosci.*, **7**, 355–360.
- Aramendía, M., Rello, L., Bérail, S., Donnard, A., Pécheyran, C. and Resano, M. (2015) Direct analysis of dried blood spots by femtosecond-laser ablation-inductively coupled plasma-mass spectrometry. Feasibility of split-flow laser ablation for simultaneous trace element and isotopic analysis. *J. Anal. At. Spectrom.*, **30**, 296–309.
- Beaudoin, N., Bellahsen, N., Lacombe, O., Emmanuel, L. and Pironon, J. (2014) Crustal-scale fluid flow during the tectonic evolution of the Bighorn Basin (Wyoming, USA). *Basin Res.*, **26**, 403–435.
- Beaudoin, N., Hamilton, A., Koehn, D., Shipton, Z.K. and Kelka, U. (2018) Reaction-induced porosity fingering: Replacement dynamic and porosity evolution in the KBr-KCl system. *Geochim. Cosmochim. Acta*, **232**, 163–180.
- Breesch, L., Swennen, R., Vincent, B., Ellison, R. and Dewever, B. (2010) Dolomite cementation and recrystallisation of sedimentary breccias along the Musandam Platform margin (United Arab Emirates). *J. Geochem. Explor.*, **106**, 34–43.
- Castéras, M., Canérot, J., Paris, J., Tisin, D., Azambre, M., Alimen, H. (1970) *Carte géologique de la France au 1/50 000: Feuille d'Oloron Sainte Marie*. BRGM Orléans, Fr.
- Centrella, S. (2019) *The Granulite- to Eclogite- and Amphibolite-facies Transition: A Volume and Mass Transfer Study in the Lindås Nappe, Bergen Arcs, West Norway*. Geological Society, London, Special Publications, From: FERRERO, S., LANARI, P., GONCALVES, P. & GROSCHE, E. G. (eds) *Metamorphic Geology: Microscale to Mountain Belts* 241–263.
- Centrella, S., Austrheim, H. and Putnis, A. (2015) Coupled mass transfer through a fluid phase and volume preservation during the hydration of granulite: An example from the Bergen Arcs, Norway. *Lithos*, **236–237**, 245–255.
- Centrella, S., Austrheim, H. and Putnis, A. (2016) Mass transfer and trace element redistribution during hydration of granulites in the Bergen Arcs, Norway. *Lithos*, **262**, 1–10.
- Centrella, S., Putnis, A., Lanari, P. and Austrheim, H. (2018) Textural and chemical evolution of pyroxene during hydration and deformation: A consequence of retrograde metamorphism. *Lithos*, **296–299**, 245–264.
- Chen, Y., Chu, X.L., Zhang, X.L. and Zhai, M.G. (2015) Carbon isotopes, sulfur isotopes, and trace elements of the dolomites from the Dengying Formation in Zhenba area, southern Shaanxi: Implications for shallow water redox

- conditions during the terminal Ediacaran. *Sci. China Earth Sci.*, **58**, 1107–1122.
- Chen, Y.-X., Schertl, H.-P., Zheng, Y.-F., Huang, F., Zhou, K. and Gong, Y.-Z. (2016) Mg–O isotopes trace the origin of Mg-rich fluids in the deeply subducted continental crust of Western Alps. *Earth Planet Sci. Lett.*, **456**, 157–167.
- Corre, B., Lagabriele, Y., Labaume, P., Fourcade, S., Clerc, C. and Ballèvre, M. (2016) Deformation associated with mantle exhumation in a distal, hot passive margin environment: New constraints from the Saraillé Massif (Châinons Béarnais, North-Pyrenean Zone). *Comptes. Rendus. Geoscience.*, **348**, 279–289.
- Debure, M., Lassin, A., Marty, N.C., Claret, F., Virgone, A., Calassou, S. and Gaucher, E.C. (2019) Thermodynamic evidence of giant salt deposit formation by serpentinization: an alternative mechanism to solar evaporation. *Sci. Rep.*, **9**, 11720.
- Deininger, R.W. (1964) *Ferrous iron and uranium concentrations and distributions in 100 selected limestones and dolomites*. Dissertation. Rice University, Houston, TX.
- Diehl, S.F., Hofstra, A.H., Koenig, A.E., Emsbo, P., Christiansen, W. and Johnson, C. (2010) Hydrothermal zebra dolomite in the Great Basin, Nevada - Attributes and relation to Paleozoic stratigraphy, tectonics, and ore deposits. *Geosphere*, **6**, 665–690.
- Donard, A., Pointurier, F., Pottin, A.-C., Hubert, A. and Pécheyran, C. (2017) Determination of the isotopic composition of micrometric uranium particles by UV femtosecond laser ablation coupled with sector-field single-collector ICP-MS. *J. Anal. At. Spectrom.*, **32**, 96–106.
- Eriksen, F.K., Toussaint, R., Måløy, K.J. and Flekkøy, E.G. (2015) Invasion patterns during two-phase flow in deformable porous media. *Front. Phys.*, **3**, 312.
- Feldkamp, L.A., Davis, L.C. and Kress, J.W. (1984) Practical cone-beam algorithm. *J. Optic. Soc. Am.*, **1**, 612–619.
- Gasparrini, M., Bechstdt, T. and Boni, M. (2006) Massive hydrothermal dolomites in the southwestern Cantabrian Zone (Spain) and their relation to the Late Variscan evolution. *Mar. Pet. Geol.*, **23**, 543–568.
- Golfier, F., Zarcone, C., Bazin, B., Lenormand, R., Lasseux, D. and Quintard, M. (2002) On the ability of a Darcy-scale model to capture wormhole formation during the dissolution of a porous medium. *J. Fluid Mech.*, **457**, 213–254.
- Gomez-Rivas, E., Corbella, M., Martín-Martín, J.D., Stafford, S.L., Teixell, A., Bons, P.D., Griera, A. and Cardellach, E. (2014) Reactivity of dolomitizing fluids and Mg source evaluation of fault-controlled dolomitization at the Benicàssim outcrop analogue (Maestrat basin, E Spain). *Mar. Pet. Geol.*, **55**, 26–42.
- Graf, D.L. (1961) Crystallographic tables for the rhombohedral carbonates. *Am. Miner.*, **46**, 1283–1316.
- Gresens, R.L. (1967) Composition-Volume relationships of metasomatism. *Chem. Geol.*, **2**, 47–65.
- Haskin, L. and Gehl, M.A. (1962) The Rare-Earth distribution in sediments. *J. Geophys. Res.*, **67**, 2537–2541.
- Henderson, P. (1984) Chapter 1 - General Geochemical Properties and Abundances of the Rare Earth Elements. In: *Rare Earth Element Geochemistry* (Ed. Henderson, P.), *Developments in Geochemistry*, **2**, 1–32.
- Hermann, J., Zheng, Y.-F. and Rubatto, D. (2013) Deep Fluids in Subducted Continental Crust. *Elements*, **9**, 281–287.
- Huang, J., Chu, X., Jiang, G., Feng, L. and Chang, H. (2011) Hydrothermal origin of elevated iron, manganese and redox-sensitive trace elements in the c. 635 Ma Doushantuo cap carbonate. *J. Geol. Soc.*, **168**, 805–816.
- Incerpi, N., Manatschal, G., Martire, L., Bernasconi, S.M., Gerdes, A. and Bertok, C. (2020) Characteristics and timing of hydrothermal fluid circulation in the fossil Pyrenean hyperextended rift system: new constraints from the Châinons Béarnais (W Pyrenees). *Int. J. Earth. Sci.*, **110**, 1.
- Izquierdo-Llavall, E., Menant, A., Aubourg, C., Callot, J.-P., Hoareau, G., Lahfid, A., Camps, P. and Pere, E. (2020) Pre-orogenic folds and syn-orogenic basement tilts in an inverted hyperextended margin : the northern Pyrenees case study. *Tectonics*, **39**.
- James, V. (1998) *La Plate-forme Carbonatée Ouest-Pyrénéenne au Jurassique Moyen et Supérieur*. PhD. Toulouse: Université Paul Sabatier, 355 pp.
- Jamtveit, B., Austrheim, H. and Malthe-Sørenssen, A. (2000) Accelerated hydration of the Earth's deep crust induced by stress perturbations. *Nature*, **408**, 75–78.
- Jamtveit, B. and Hammer, Ø. (2012) Sculpting of Rocks by Reactive Fluids. *Geochem. Persp.*, **1**, 341–481.
- Jamtveit, B., Malthe-Sørenssen, A. and Kostenko, O. (2008) Reaction enhanced permeability during retrogressive metamorphism. *Earth Planet Sci. Lett.*, **267**, 620–627.
- Jochum, K.P., Weis, U., Stoll, B., Kuzmin, D., Yang, Q., Raczek, I., Jacob, D.E., Stracke, A., Birbaum, K., Frick, D.A., Günther, D. and Enzweiler, J. (2011) Determination of Reference Values for NIST SRM 610–617 Glasses Following ISO Guidelines. *Geostand. Geoanal. Res.*, **35**, 397–429.
- Jochum, K.P., Wilson, S.A., Abouchami, W., Amini, M., Chmieleff, J., Eisenhauer, A., Hegner, E., Iaccheri, L.M., Kieffer, B., Krause, J., McDonough, W.F., Mertz-Kraus, R., Raczek, I., Rudnick, R.L., Scholz, D., Steinhöfel, G., Stoll, B., Stracke, A., Tonarini, S., Weis, D., Weis, U. and Woodhead, J.D. (2010) GSD-1G and MPI-DING Reference Glasses for In Situ and Bulk Isotopic Determination. *Geostand. Geoanal. Res.*, **35**, 193–226.
- Jonas, L., Müller, T., Dohmen, R., Baumgartner, L. and Putlitz, B. (2015) Transport-controlled hydrothermal replacement of calcite by Mg-carbonates. *Geology*, **43**, 779–782.
- Jonas, L., Müller, T., Dohmen, R., Immenhauser, A. and Putlitz, B. (2017) Hydrothermal replacement of biogenic and abiogenic aragonite by Mg-carbonates – Relation between textural control on effective element fluxes and resulting carbonate phase. *Geochim. Cosmochim. Acta*, **196**, 289–306.
- Kar, A., Chiang, T.-Y., Ortiz Rivera, I., Sen, A. and Velegol, D. (2015) Enhanced transport into and out of dead-end pores. *ACS Nano*, **9**, 746–753.
- Kelemen, P.B. and Hirth, G. (2012) Reaction-driven cracking during retrograde metamorphism: Olivine hydration and carbonation. *Earth Planet Sci. Lett.*, **345–348**, 81–89.
- Kelka, U. (2017) *Pattern Formation in Mississippi Valley-Type Deposits - Identifying one of Nature's Fundamental Processes in Geologic Systems*. PhD thesis. School of Geographical and Earth Sciences, College of Science and Engineering, University of Glasgow, Glasgow, 355 pp.
- Kelka, U., Koehn, D. and Beaudoin, N. (2015) Zebra pattern in rocks as a function of grain growth affected by second-phase particles. *Front. Phys.*, **3**, 201.
- Kelka, U., Veveakis, M., Koehn, D. and Beaudoin, N. (2017) Zebra rocks: compaction waves create ore deposits. *Sci Rep*, **7**, 14260.

- Kirschner, J.P. and Barnes, D.A. (2009) Geological sequestration capacity of the Dundee Limestone, Michigan Basin, United States. *Environ. Geosci.*, **16**, 127–138.
- Koeshidayatullah, A., Corlett, H., Stacey, J., Swart, P.K., Boyce, A. and Hollis, C. (2020b) Origin and evolution of fault-controlled hydrothermal dolomitization fronts: A new insight. *Earth Planet. Sci. Lett.*, **541**, 116291.
- Koeshidayatullah, A., Corlett, H., Stacey, J., Swart, P.K., Boyce, A., Robertson, H., Whitaker, F. and Hollis, C. (2020a) Evaluating new fault-controlled hydrothermal dolomitization models: Insights from the Cambrian Dolomite, Western Canadian Sedimentary Basin. *Sedimentology*, **26**, 515.
- Kondratiuk, P., Tredak, H., Ladd, A.J.C. and Szymczak, P. (2015) Synchronization of dissolution and precipitation fronts during infiltration-driven replacement in porous rocks. *Geophys. Res. Lett.*, **42**, 2244–2252.
- Krug, H.-J., Brandstatter, H. and Jacob, K.H. (1996) Morphological instabilities in pattern formation by precipitation and crystallization processes. *Geol. Rundsch.*, **85**, 19–28.
- Labauume, P. and Teixell, A. (2020) Evolution of salt structures of the Pyrenean rift (Chanons Barnais, France): From hyper-extension to tectonic inversion. *Tectonophysics*, **785**.
- Lagabrielle, Y., Labauume, P., and de Saint Blanquat, M. (2010) Mantle exhumation, crustal denudation, and gravity tectonics during Cretaceous rifting in the Pyrenean realm (SW Europe): Insights from the geological setting of the lherzolite bodies. *Tectonics*, **29**, 1–26.
- Lanari, P., Vho, A., Bovay, T., Airaghi, L. and Centrella, S. (2019) *Quantitative Compositional Mapping of Mineral Phases by Electron Probe Micro-Analyser*. Geological Society, London, Special Publications, From: FERRERO, S., LANARI, P., GONCALVES, P. & GROSCHE, E. G. (eds) *Metamorphic Geology: Microscale to Mountain Belts*, 478, 39–63.
- Lanari, P., Vidal, O., De Andrade, V., Dubacq, B., Lewin, E., Grosch, E. G. and Schwartz, S. (2014) XMapTools: A MATLAB-based program for electron microprobe X-ray image processing and geothermobarometry. *Comput. Geosci.*, **62**, 227–240.
- Leach, D.L. and Viets, J.G. (1992) Comparison of the Cracow-Silesian Mississippi valley-type district, southern Poland, with Mississippi valley-type districts in North America. Open-File Report.
- Lenoble, J.-L. (1992) *Les Plantes-formes Carbonates Ouest Pyrennennes du Dogger  l’Albien*. PhD. Toulouse: Universit Paul Sabatier, 447 pp.
- Ling, H.-F., Chen, X., Li, D., Wang, D., Shields-Zhou, G.A. and Zhu, M. (2013) Cerium anomaly variations in Ediacaran–earliest Cambrian carbonates from the Yangtze Gorges area, South China: Implications for oxygenation of coeval shallow seawater. *Precamb. Res.*, **225**, 110–127.
- Machel, H.G. (2004) *Concepts and Models of Dolomitization: a Critical Reappraisal*. Geological Society, London, Special Publications, From: BRAITHWAITE, C. J. R., RIZZI, G. & DARKE, G. (eds) 2004. *The Geometry and Petrogenesis of Dolomite Hydrocarbon Reservoirs*. Geological Society, London, Special Publications, 235, 7–63.
- Machel, H.G. and Lonnee, J. (2002) Hydrothermal dolomite —a product of poor definition and imagination. *Sed. Geol.*, **152**, 163–171.
- Machel, H.G. and Mountjoy, E.W. (1986) Chemistry and environments of dolomitization - A reappraisal. *Earth-Sci. Rev.*, **23**, 175–222.
- Martn-Martn, J.D., Trav, A., Gomez-Rivas, E., Salas, R., Sizun, J.-P., Vergs, J., Corbella, M., Stafford, S.L. and Alfonso, P. (2015) Fault-controlled and stratabound dolostones in the Late Aptian–earliest Albian Benassal Formation (Maestrat Basin, E Spain): Petrology and geochemistry constrains. *Mar. Pet. Geol.*, **65**, 83–102.
- Masini, E., Manatschal, G., Tugend, J., Mohn, G. and Flament, J.-M. (2014) The tectono-sedimentary evolution of a hyper-extended rift basin: the example of the Arzacq-Maulon rift system (Western Pyrenees, SW France). *Int. J. Earth. Sci. (Geol. Rundsch.)*, **103**, 1569–1596.
- Merino, E. and Canals, A. (2011) Self-accelerating dolomite for calcite replacement: self organized dynamics of burial dolomitization and associated mineralization. *Am. J. Sci.*, **311**, 573–607.
- Montes-Hernandez, G., Renard, F., Auzende, A.-L. and Findling, N. (2020) Amorphous Calcium-Magnesium Carbonate (ACMC) Accelerates Dolomitization at Room Temperature under Abiotic Conditions. *Cryst. Growth. Des.*, **20**, 1434–1441.
- Mouthereau, F., Filleaudeau, P.-Y., Vacherat, A., Pik, R., Lacombe, O., Fellin, M.G., Castellort, S., Christophoul, F. and Masini, E. (2014) Placing limits to shortening evolution in the Pyrenees: Role of margin architecture and implications for the Iberia/Europe convergence. *Tectonics*, **33**, 2283–2314.
- Mozafari, M., Swennen, R., Balsamo, F., El Desouky, H., Storti, F. and Taberner, C. (2019) Fault-controlled dolomitization in the Montagna dei Fiori Anticline (Central Apennines, Italy): record of a dominantly pre-orogenic fluid migration. *Solid Earth*, **10**, 1355–1383.
- Nader, F.H., Lpez-Horgue, M.A., Shah, M.M., Dewit, J., Garcia, D., Swennen, R., Iriarte, E., Muchez, P. and Caline, B. (2012) The Ranero Hydrothermal Dolomites (Albian, Karrantza Valley, Northwest Spain): Implications on Conceptual Dolomite Models. *Oil & Gas Sci. Technol.*, **67**, 9–29.
- Palink, S.S., Spangenberg, J.E. and Palink, L.A. (2009) Organic and inorganic geochemistry of Ljubija siderite deposits, NW Bosnia and Herzegovina. *Miner. Deposita*, **44**, 893–913.
- Paradis, S., Hannigan, P. and Dewing, K. (2007) Mississippi Valley-type lead-zinc deposits (MVT). In: *Mineral Deposits of Canada: A Synthesis of Major Deposit-Types, District Metallogeny, the Evolution of Geological Provinces, and Exploration Methods* (Ed. Goodfellow, W.D.), Geological Association of Canada, Mineral Deposits Division, Special Publication, **5**, 185–203.
- Paton, C., Hellstrom, J., Paul, B., Woodhead, J. and Hergt, J. (2011) Lolite: Freeware for the visualisation and processing of mass spectrometric data. *J. Anal. At. Spectrom.*, **26**, 2508.
- Pearce, M.A., Timms, N.E., Hough, R.M. and Cleverley, J.S. (2013) Reaction mechanism for the replacement of calcite by dolomite and siderite: implications for geochemistry, microstructure and porosity evolution during hydrothermal mineralisation. *Contrib. Mineral. Petrol.*, **166**, 995–1009.
- Pedrosa, E.T., Putnis, C.V. and Putnis, A. (2016a) The pseudomorphic replacement of marble by apatite: The role of fluid composition. *Chem. Geol.*, **425**, 1–11.
- Pedrosa, E.T., Putnis, C.V., Renard, F., Burgos-Cara, A., Laurich, B. and Putnis, A. (2016b) Porosity generated during the fluid-mediated replacement of calcite by fluorite. *Cryst. Eng. Comm.*, **18**, 6867–6874.

- Peters, D. and Pettke, T. (2017) Evaluation of Major to Ultra Trace Element Bulk Rock Chemical Analysis of Nanoparticulate Pressed Powder Pellets by LA-ICP-MS. *Geostand. Geoanal. Res.*, **41**, 5–28.
- Pinto, V.H.G., Manatschal, G., Karpoff, A.M., Ulrich, M. and Viana, A.R. (2017) Seawater storage and element transfer associated with mantle serpentinization in magma-poor rifted margins: A quantitative approach. *Earth Planet Sci. Lett.*, **459**, 227–237.
- Piper, D.Z. (1974) Rare earth elements in the sedimentary cycle: A summary. *Chem. Geol.*, **14**, 285–304.
- Puigdefàbregas, C. and Souquet, P. (1986) Tecto-sedimentary cycles and depositional sequences of Mesozoic and Tertiary from the Pyrenees. *Tectonophysics*, **129**, 173–203.
- Putnis, A. (2002) Mineral replacement reactions: from macroscopic observations to microscopic mechanisms. *Mineral. Mag.*, **66**, 689–708.
- Putnis, A. (2009) Mineral replacement reactions. *Rev. Mineral. Geochem.*, **70**, 87–124.
- Putnis, A. and Putnis, C.V. (2007) The mechanism of reequilibration of solids in the presence of a fluid phase. *J. Solid. State. Chem.*, **180**, 1783–1786.
- Putnis, C.V. and Mezger, K. (2004) A mechanism of mineral replacement: isotope tracing in the model system KCl-KBr-H₂O. *Geochim. Cosmochim. Acta*, **68**, 2839–2848.
- Putnis, C.V., Tsukamoto, K. and Nishimura, Y. (2005) Direct observations of pseudomorphism: compositional and textural evolution at a fluid-solid interface. *Am. Miner.*, **90**, 1909–1912.
- Quesnel, Benoît, Boiron, Marie-Christine, Cathelineau, Michel, Truche, Laurent, Rigaudier, Thomas, Bardoux, Gérard, Agrinier, Pierre, de Saint Blanquat, Michel, Masini, Emmanuel and Gaucher, Eric C., (2019) Nature and origin of mineralizing fluids in hyperextensional systems: The case of cretaceous Mg metasomatism in the pyrenees. *Geofluids*, **2019**, 1–18.
- Ramachandran, G.N. and Lakshminarayanan, A.V. (1971) Three-dimensional Reconstruction from Radiographs and Electron Micrographs Application of Convolutions instead of Fourier Transforms. *Proc. Natl. Acad. Sci. USA*, **68**, 2236–2240.
- Raufaste, C., Jamtveit, B., John, T., Paul, M. and Dysthe, D. (2011) The mechanism of porosity formation during solvent-mediated phase transformations. *Proc. R. Soc. A*, **467**, 1408–1426.
- Ruiz-Agudo, E., Putnis, C.V. and Putnis, A. (2014) Coupled dissolution and precipitation at mineral–fluid interfaces. *Chem. Geol.*, **383**, 132–146.
- Salardon, R., Carpentier, C., Bellahsen, N., Pironon, J. and France-Lanord, C. (2017) Interactions between tectonics and fluid circulations in an inverted hyper-extended basin: Example of Mesozoic carbonate rocks of the western North Pyrenean Zone (Châlonnais Béarnais, France). *Mar. Pet. Geol.*, **80**, 563–586.
- Scribano, V., Carbone, S., Manuella, F.C., Hovland, M., Rueslåtten, H. and Johnsen, H.-K. (2017) Origin of salt giants in abyssal serpentinite systems. *Int. J. Earth Sci. (Geol. Rundsch)*, **106**, 2595–2608.
- Slaughter, M. and Hill, R.J. (1991) The Influence of Organic Matter in Organogenic Dolomitization: PERSPECTIVE. *J. Sediment. Petrol.*, **61**, 296–303.
- Steinfink, H. and Sans, F.J. (1959) Refinement of the crystal structure of dolomite. *Am. Miner.*, **44**, 679–682.
- Swennen, R., Dewit, J., Fierens, E.L.S., Mucchez, P., Shah, M., Nader, F. and Hunt, D. (2012) Multiple dolomitization events along the Pozalagua Fault (Pozalagua Quarry, Basque-Cantabrian Basin, Northern Spain). *Sedimentology*, **59**, 1345–1374.
- Szymczak, P. and Ladd, A.J.C. (2006) A network model of channel competition in fracture dissolution. *Geophys. Res. Lett.*, **33**, 45.
- Szymczak, P. and Ladd, A.J.C. (2014) Reactive-infiltration instabilities in rocks. Part 2. Dissolution of a porous matrix. *J. Fluid Mech.*, **738**, 591–630.
- Teixell, A., Labaume, P. and Lagabriele, Y. (2016) The crustal evolution of the west-central Pyrenees revisited: Inferences from a new kinematic scenario. *CR Geosci.*, **348**, 257–267.
- Thibeau, S., Chiquet, P., Prinnet, C. and Lescanne, M. (2013) Lacq-Rousse CO₂ Capture and Storage Demonstration Pilot: Lessons Learnt from Reservoir Modelling Studies. *Energy Procedia*, **37**, 6306–6316.
- Tugend, J., Manatschal, G. and Kusznir, N.J. (2015) Spatial and temporal evolution of hyperextended rift systems: Implication for the nature, kinematics, and timing of the Iberian-European plate boundary. *Geology*, **43**, 15–18.
- Vacherat, A., Mouthereau, F., Pik, R., Bernet, M., Gautheron, C., Masini, E., Le Pourhiet, L., Tibari, B. and Lahfid, A. (2014) Thermal imprint of rift-related processes in orogens as recorded in the Pyrenees. *Earth Planet Sci. Lett.*, **408**, 296–306.
- Wallace, M.W., Both, R.A., Ruano, S.M., Fenoll Hach-Ali, P. and Lees, T. (1994) Zebra textures from carbonate-hosted sulfide deposits; sheet cavity networks produced by fracture and solution enlargement. *Econ. Geol.*, **89**, 1183–1191.
- Warren, J. (2000) Dolomite: occurrence, evolution and economically important associations. *Earth-Sci. Rev.*, **52**, 1–81.
- Welte, D.H. (1962) Sedimentologische Untersuchung uranhaltiger Keupersedimente aus der Umgebung von Lichtenfels bei Coburg. *Geol. Bavarica*, **49**, 91–123.
- Wheeler, J. (1987) The significance of grain-scale stresses in the kinetics of metamorphism. *Contrib. Miner. Petrol.*, **97**, 397–404.
- Whitaker, F.F., Smart, P.L. and Jones, G.D. (2004) Dolomitization: from conceptual to numerical models. In: *The Geometry and Petrogenesis of Dolomite Hydrocarbon Reservoirs* (Eds Braithwaite, C.J.R., Rizzi, G. and Darke, G.), *Geological Society, London, Special Publications*, **235**, 99–139.
- White, W. (2013) *Geochemistry*, 55 pp.
- Wilson, E.N., Hardie, L.A. and Phillips, O.M. (1990) Dolomitization front geometry, fluid flow patterns, and the origin of massive dolomite the Triassic Latemar buildup northern Italy. *Am. J. Sci.*, **290**, 741–796.
- Xu, L., Marks, B., Toussaint, R., Flekkøy, E.G. and Måløy, K.J. (2018) Dispersion in fractures with ramified dissolution patterns. *Front. Phys.*, **6**, 186.
- Zhang, W., Guan, P., Jian, X., Feng, F. and Zou, C. (2014) In situ geochemistry of Lower Paleozoic dolomites in the northwestern Tarim basin: Implications for the nature, origin, and evolution of diagenetic fluids. *Geochim. Geophys. Geosyst.*, **15**, 2744–2764.
- Zhou, C.M., Jiang, S.Y., Xiao, S.H., Chen, Z. and Yuan, X.L. (2012) Rare earth elements and carbon isotope geochemistry of the Doushantuo Formation in South China: Implication for middle Ediacaran shallow marine redox conditions. *Chin. Sci. Bull.*, **57**, 1998–2006.

Manuscript received 31 March 2020; revision 28 September 2020; revision accepted 1 October 2020

Supporting Information

Additional information may be found in the online version of this article:

Figure S1. Outcrop showing the contact between the original limestone and the dolomite.

Figure S2. Pole figures lower hemispheres showing that none of the phases shows any crystal preferred orientation. All hemispheres have a half width 10° and a cluster size 5° .

Figure S3. Box plot of the respective volume of the porosity and grain size area for dolomite and calcite (μm^2) across the hand specimen.

Table S1. Microprobe analyses of calcite and dolomite (wt.%). Structural formula has been calculated normalized to two oxygens.

Table S2. Results of trace elements content by LA-ICP-MS (laser ablation inductively coupled plasma mass spectrometry) (ppm) and 2 se (two standard error).